

Mechanism of Low Pressure Plasma-Assisted CO₂ Hydrogenation Over Ni-USY by Microsecond Time-resolved FTIR Spectroscopy

Federico Azzolina-Jury¹ · Frédéric Thibault-Starzyk¹

Published online: 10 August 2017
© Springer Science+Business Media, LLC 2017

Abstract Zeolite H-USY doped with nickel (14% wt.) was used as a catalyst in the plasma-assisted CO₂ hydrogenation under partial vacuum. CO was found to be the main product of the reaction and it is generated by plasma-assisted CO₂ dissociation in the gas phase. The CO₂ molecules vibrationally excited by plasma are also adsorbed on metallic nickel as formates which are further transformed into linear carbonyls. These species are then hydrogenated to form methane. Since the catalyst presents a low basic behavior, methane is produced from hydrogenation of linear carbonyls on nickel surface rather than from carbonates species. A detailed mechanism for this reaction assisted by plasma (glow discharge) is proposed using Operando time-resolved FTIR spectroscopic data.

Keywords Mechanism · CO₂ hydrogenation · Time-resolved FTIR · Glow discharge · Zeolite USY

1 Introduction

Carbon dioxide (CO₂) concentration in the atmosphere has been increasing since the end of the industrial revolution and it is a well-known issue that contributes to the greenhouse effect. Thermal CO₂ hydrogenation has been proposed and

studied by many researchers during the last decades as a contribution to the solution to global warming. Therefore, CO₂ can be used as a chemical reactant and be valorized into carbon monoxide (CO) and methane (CH₄) as main products. CH₄ can be further used as synthetic natural gas (SNG) creating a global cycle between CH₄ combustion and CO₂ methanation [1]. CO (CO-rich syngas) can be used as reactant for Fischer–Tropsch reaction for synthesizing hydrocarbons as well as for manufacturing a wide range of products such as olefins, paraffins and oxygenated products (e.g. aldehydes, alcohols, acids and ketones) [2–5].

Transition metals have been usually adopted as catalysts for thermal CO₂ hydrogenation. The choice of transition metal can significantly affect the product distribution of this reaction. Depending on the thermal reaction conditions, Ni [6, 7] and Ru [8, 9] catalysts produce mainly CH₄ while Pd [10], Pt [11], Rh [12], Mo [13] and Au [14] favor CH₄, CO and methanol (CH₃OH) production. Cu [15] can be used to produce mainly CH₃OH. Nickel has been reported to be the most interesting catalyst for thermal CO₂ hydrogenation due to its high activity and low cost [1, 16].

The catalyst support also plays a key role on thermal catalysis through the active phase dispersion, activity and stability. Thermal CO₂ hydrogenation has been studied over a wide range of supports such as Al₂O₃ [17], SiO₂ [11], TiO₂ [11] and Ce–Zr mixed oxides [16]. Zeolites with high surface area and stability are very attractive supports. Ni-doped ultra-stable faujasites (USY) have been reported to present higher stability and comparable thermal catalytic activity with respect to the best thermal CO₂ hydrogenation catalysts found in the literature [1].

Nevertheless, thermal CO₂ hydrogenation catalysts are only active at high temperatures near 450 °C. Under high-temperature working conditions and atmospheric pressure, the catalysts are deactivated by poisoning (coke deposition)

Electronic supplementary material The online version of this article (doi:10.1007/s11244-017-0849-2) contains supplementary material, which is available to authorized users.

✉ Federico Azzolina-Jury
federico.azzolina-jury@ensicaen.fr

¹ Laboratoire Catalyse et Spectrochimie (LCS), CNRS-ENSICAEN-Université de Caen, 6 boulevard du Maréchal-Juin, 14050 Caen, France

and sintering of the active phase. This drawback decreases the industrial viability of the CO₂ hydrogenation processes under thermal heating.

Carbon dioxide hydrogenation can be intensified by using plasma technology. Plasmas provide very high concentrations of energetic and chemically active species such as electrons, ions, atoms, radicals and excited species at relatively low temperatures near room temperature. The use of low pressure plasmas is preferred for several reasons: (i) the plasma is stable; (ii) the catalyst deactivation by coke deposition is thermodynamically minimized; (iii) the reaction rate is increased compared to thermal heating and thermodynamic CO₂ conversion and products yield can be easily overcome and (iv) the lifetime of excited species is prolonged [18, 19]. Some disadvantages related to low pressure systems can be also cited such as (i) higher operating costs associated to the vacuum system; (ii) higher risk of system contamination in case of leaks and (iii) adsorption phenomena are more difficult at low pressure. Hence, under low pressure conditions, CH₄ selectivity and yield is lower than those found in literature under atmospheric pressure.

As in thermal catalysis, the catalyst support plays also a key role in plasma-assisted catalysis. The phenomena responsible for the synergistic effects in the interaction between the catalyst support and the plasma have been recently investigated. Various plasma effects on the catalyst as well as several catalyst support effects on the plasma have been proposed in the literature in order to explain the plasma–catalysis synergistic effects from theoretical modelling [20–22]. Moreover, an excellent review about the current state of knowledge and ignorance on plasma–catalysis interaction mechanisms has recently been published [23].

Nevertheless, CO₂ hydrogenation reaction mechanism has been widely studied using several sorts of catalysts and supports under thermal heating only [1, 16, 24–35]. A few papers have been recently reported on the plasma-assisted CO₂ dissociation [36, 37] but, to the best of our knowledge, there is no scientific research dealing with plasma-assisted CO₂ hydrogenation reaction mechanism.

In this work, the low pressure plasma-assisted mechanism of CO₂ hydrogenation is studied by time-resolved FTIR. A low pressure glow discharge at 50 Hz was used. Operando and in-situ infrared spectra were collected in the reactor discharge zone at 2.28 Torr. The evolution of the IR bands intensities of the species in the gas phase as well as of the adsorbed species (intermediates) on Ni-USY is reported at the microsecond time-scale.

2 Experimental

2.1 Catalyst Preparation

The ultra-stable faujasite protonic zeolite (H-USY) with Si/Al molar ratio of 40 was supplied by Grace Davison. Nickel introduction on the zeolite support was carried out by wet impregnation (14 wt.%), using nickel nitrate hexahydrate [Ni(NO₃)₂·6H₂O, Merck, >99%] as precursor salt diluted in water. The water was evaporated using a rotary-evaporator at 80 °C under vacuum until complete dryness. Afterward, the zeolite Ni-USY was treated under N₂ flow (25 NmL min⁻¹) at 500 °C during 10 h followed by calcination in air at 500 °C for 3 h. Finally, zeolite powders were pressed (5 × 10⁷ Pa) into self-supported wafers (2 cm², ~20 mg) for infrared measurements. Notice that, in this work, the gas flow rates are expressed as normal milliliters per minute (NmL min⁻¹), since the gas flow rate values are calculated at normal temperature and pressure conditions: temperature = 273 K and Pressure = 760 Torr.

2.2 Catalyst Characterization

2.2.1 Verification of Crystalline Structure

The crystallinity of zeolite Ni-USY was verified with a PANalytical X'Pert PRO diffractometer with CuK α radiation ($\lambda = 0.15418$ nm, 40 mA, 45 kV). The diffraction data were collected between 5° and 50° of 2 θ at intervals of 0.1° and speed of 2° per min.

2.2.2 Determination of Zeolite Surface Area, Microporous and Mesoporous Volumes

The specific surface area and pore volume of the Ni-USY zeolite were determined by N₂ adsorption–desorption measurements at 77 K using the Brunauer–Emmet–Teller (BET) and T-plot methods respectively in a Micrometrics sorptionometer Tri Star 3000. Before N₂ adsorption, the samples were outgassed at 200 °C overnight.

2.2.3 Scanning Electron Microscopy of Zeolite Catalyst

The size and morphology of the zeolite crystals and nickel particles were examined with a Philips XL-30 scanning electron microscope (SEM) with acceleration voltage of 30 kV.

2.2.4 Temperature-Programmed Reduction Under Vacuum (TPR-MS)

After calcination, the reduction of zeolite Ni-USY was performed in-situ before reaction (in the same experimental setup which was used for the CO₂ hydrogenation) and the

hydrogen consumption was followed by mass spectrometry (TPR-MS).

2.3 Operando Time-Resolved IR Spectroscopy Setup

The reactor designed for Operando time-resolved IR spectroscopy is presented in Fig. 1a. The sample holder containing the 20 mg catalyst wafer is placed inside the reactor within the glow discharge zone perpendicularly to the IR beam. The plasma discharge is generated between two tungsten electrodes which are connected to a high voltage ac power supply (Resinblock transformer FART, 50 mA) with a maximum voltage and frequency of 2 kV and 50 Hz, respectively. The gas inlet with mass flow controllers (Brooks) is located on the top of the reactor. The gas outlet is connected to a vacuum pump and also to a Quadrupole Mass Spectrometer (Pfeiffer Omnistar GSD 301) in order to analyze the composition of the gas phase. The reactor is placed inside the sample compartment of a Bruker Vertex 80v spectrometer with a Mercury–Cadmium–Telluride MCT detector. Such spectrometer allows fast time-resolved acquisition of reproducible events (transients) by the step-scan technique. The *modus operandi* of this technique has been detailed in a previous work [38]. Once the glow discharge is ignited at 50 Hz (Plasma period: $T = 20$ ms) the interferometer mirror is held at a fixed position and the IR light intensity is recorded for

one point of the interferogram at equal intervals ($20 \mu\text{s}$) (Fig. 1b). The number of measurements for each point of the interferogram was set to 3000 points in order to improve the signal/noise ratio (S/N). Therefore, the residence time on each interferogram point is 60 ms corresponding to three plasma periods and six plasma pulses. The next interferogram points are recorded with same time-spaced intervals. After applying the Fourier transform to the time domain, frequency domain time-resolved spectra were obtained in the range of $4000 - 1000 \text{ cm}^{-1}$ at 32 cm^{-1} spectrum resolution.

Before starting the plasma-assisted CO_2 hydrogenation mechanism study, the catalyst was activated at 450°C during 1 h under secondary vacuum. Then, the temperature-programmed reduction of zeolite Ni-USY was performed in-situ under partial vacuum (2.8 Torr) from room temperature to 470°C . A heating rate of $10^\circ\text{C}\cdot\text{min}^{-1}$ under H_2/N_2 (5% v/v) flow of 30 NmL min^{-1} was used.

CO_2 hydrogenation was carried out using a CO_2/H_2 molar ratio of 1:4 and a volumetric flow rate of 20 NmL min^{-1} was applied. The pressure in the system was 2.1 Torr.

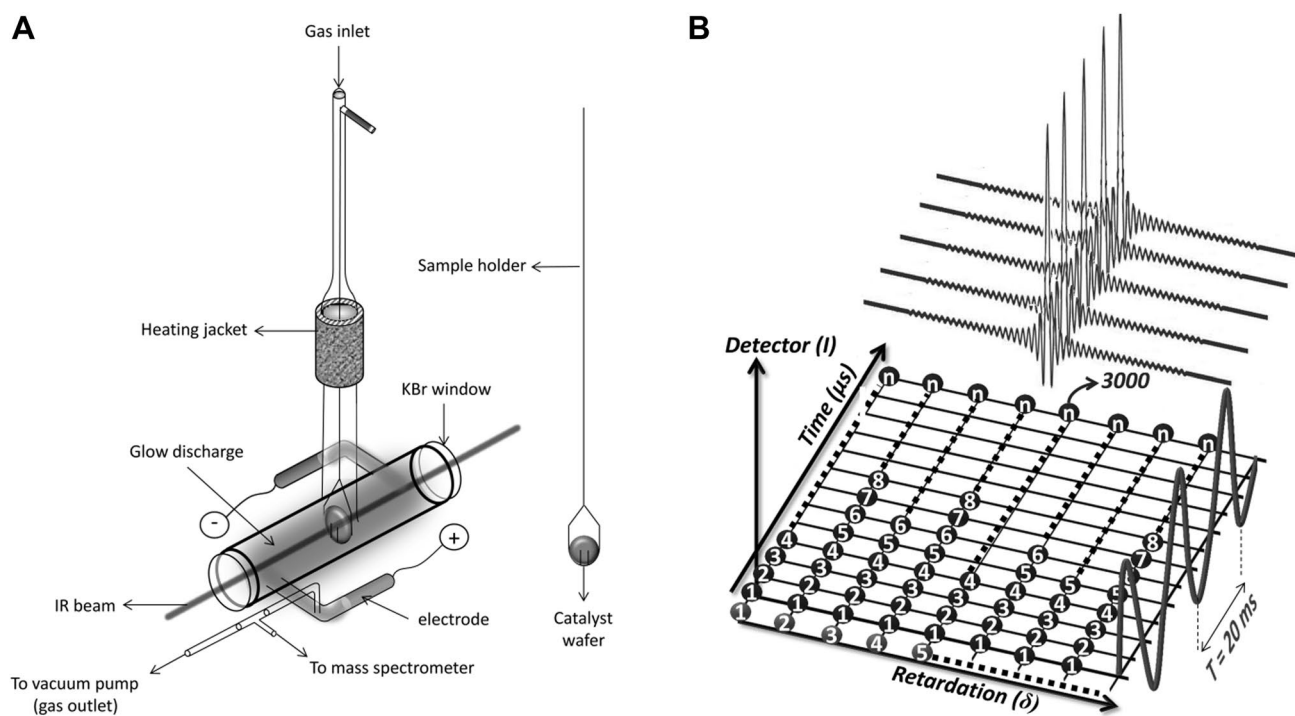


Fig. 1 **a** Operando time-resolved IR reactor; **b** step-scan acquisition of the interferogram evolution at the microsecond time-scale during glow discharge

3 Results and Discussion

3.1 Catalyst Characterization

The crystalline structure of the Ni-USY catalyst was verified by XRD. The crystallinity of the zeolite H-USY was not modified after nickel incorporation and physicochemical treatments. The Ni-USY internal and external surface areas, micropore and mesopore volumes were found to be 632 m²/g, 107 m²/g, 0.252 cm³/g and 0.201 cm³/g respectively. The SEM images of Ni-USY showed a narrow zeolite crystal size distribution of 500 nm with nickel particles of 50 nm. Nickel particles are mainly located outside the zeolite pores and the reaction takes place mainly at the catalyst surface. A low amount of nickel (as Ni²⁺) remains in the exchange position within the zeolites cages as shown by the TPR-MS profiles. Catalyst shows thus a bimodal Ni distribution with large metallic particles on the external surface and single-site centers inside the zeolite cages. The nickel dispersion in zeolite Ni-USY was calculated from in-situ TPR-MS and it was found to be equal to 17.6%.

3.2 Plasma-Assisted CO₂ Hydrogenation Mechanism

This section deals with the identification of the IR bands of the species in the gas phase as well as the adsorbed species on the catalyst in order to identify them afterwards during the microsecond time-resolved FTIR spectroscopy experiments. Hence, this section has been divided into four Sub-sections: Sect. 3.2.1. identification of species (reactants and products of the reaction) in the gas phase without plasma using conventional IR spectroscopy; Sect. 3.2.2. identification of species (reactants and products of the reaction) in the gas phase with plasma using conventional IR spectroscopy; Sect. 3.2.3. identification of adsorbed species on the catalyst (Ni-USY) using conventional IR spectroscopy and Sect. 3.2.4. identification of the species in the gas phase as well as the adsorbed species on Ni-USY using time-resolved FTIR spectroscopy for mechanistic study.

The experiments were repeated several times to verify the reproducibility of the measurements.

3.2.1 Infrared Band Assignment of the CO₂ Hydrogenation Reactants and Products in the Gas Phase

The IR bands of reactants and products of CO₂ hydrogenation in the gas phase were identified by conventional IR spectroscopy analysis of a gas mixture containing pure CH₄, CO₂ and carbon monoxide (CO) in argon (Ar) without plasma. The total volumetric flow was set to 20 NmL min⁻¹ with the following gas composition: 3 NmL CO₂ min⁻¹; 1 NmL CH₄ min⁻¹; 2 NmL CO min⁻¹ and 14

NmL Ar min⁻¹. The IR spectra were acquired with two different resolutions: 1 cm⁻¹ and 32 cm⁻¹ (Fig. 2). The high resolution spectrum allows determining more precisely the IR bands of the elements in the gas phase and linking them to those observed at lower resolution (32 cm⁻¹) at which the step-scan time-resolved FTIR Spectroscopy will be further performed.

3.2.2 Infrared Band Assignment of the CO₂ Hydrogenation Species in the Gas Phase During Plasma Assistance

The IR bands of CO₂ hydrogenation species in the gas phase were identified by conventional IR spectroscopy analysis of a gas mixture containing H₂ and CO₂ as reactants in Ar. The total volumetric flow was set to 20 NmL min⁻¹ with the following gas composition: 2 NmL CO₂ min⁻¹; 8 NmL H₂ min⁻¹ and 10 NmL Ar min⁻¹. The IR spectrum (32 cm⁻¹ resolution) was acquired with and without plasma assistance (Fig. 3).

CO₂ is vibrationally excited under plasma assistance and can be further dissociated into CO in the gas phase without catalyst. The CO₂ conversion is 60% and CO is the main product with 99% selectivity. A relatively low amount of CH₄ is also generated in the gas phase. CH₄ production can only be enhanced with the presence of an appropriate catalyst. CH₄ selectivity is enhanced up to 7% and CO₂ conversion remains equal to 60% when the reaction is performed with Ni-USY catalyst.

The intensity of CO₂ ground state IR band at 2345 cm⁻¹ is decreased under plasma assistance as a consequence of the vibrational excitation of CO₂ molecules which are observed at lower frequencies (2293 cm⁻¹). Plasma can also dissociate CO₂ into CO ground state at 2165 and 2120 cm⁻¹; and vibrationally excited at 2077 and 2034 cm⁻¹. The IR band assignments of the reactants and products of CO₂ hydrogenation in the gas phase are summarized in Table 1

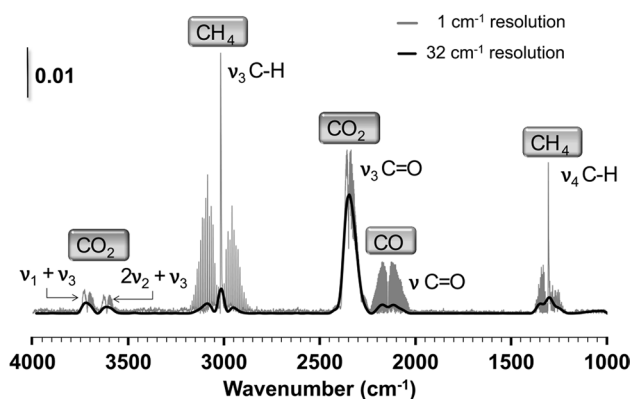


Fig. 2 IR bands of CO₂, CO and CH₄ in the gas phase

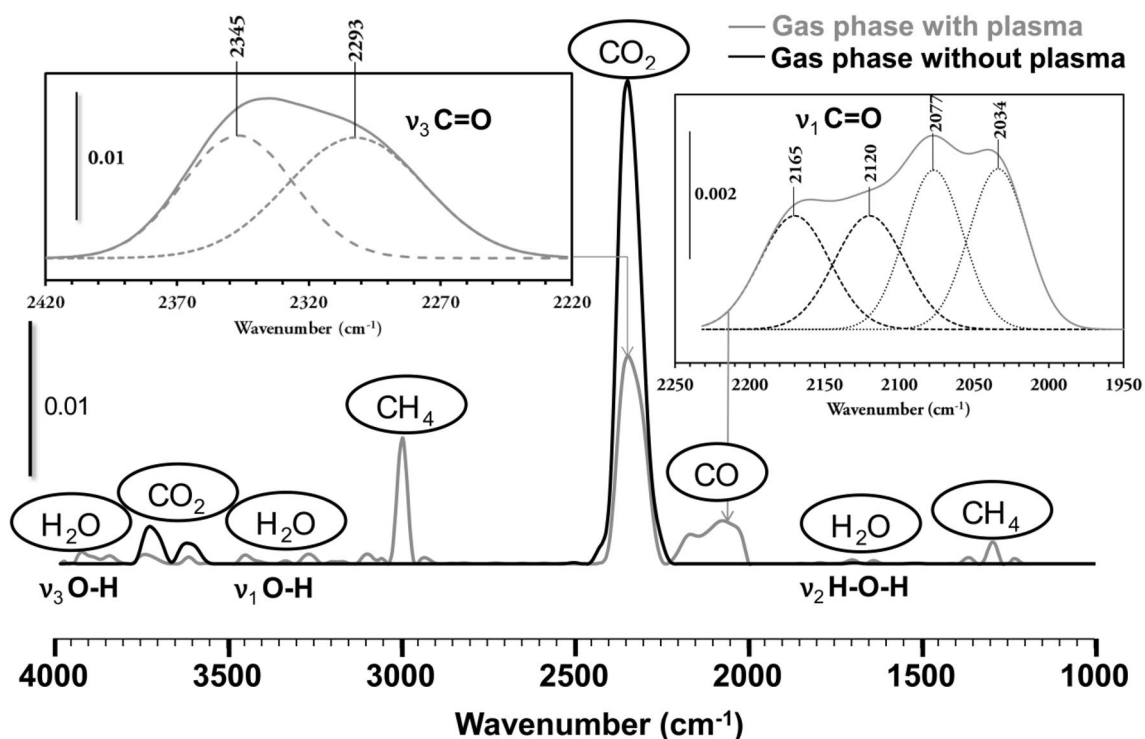


Fig. 3 IR bands of CO₂ hydrogenation species in the gas phase with and without plasma assistance

Table 1 IR band assignment of CO₂ hydrogenation reactants and products in the gas phase

Gas phase	Molecule	Mode	Band position (1 cm ⁻¹ resolution) (cm ⁻¹)	Band position (32 cm ⁻¹ resolution) (cm ⁻¹)
Without plasma	CO ₂	Combination band ($\nu_1 + \nu_3$)	3731	3723
			3701	
		Combination band ($2\nu_2 + \nu_3$)	3627	3610
			3603	
	Asymmetric stretch (ν_3)	2357	2345	
		2336		
	CH ₄	Degenerate stretch (ν_3)	3085	3085
			3017	3013
			2958	2958
		Degenerate bend (ν_4)	1332	1347
		1306	1295	
		1253	1254	
With plasma	H ₂ O	Stretch (ν_3)	2165	2165
			2120	2120
		Stretch (ν_1)	3918	3846
	3445		3260	
	Bend (ν_2)	1686	1625	
		2293	2293	
Excited CO ₂	Asymmetric stretch (ν_3)	2077	2077	
Excited CO	Stretch (ν_1)	2034	2034	

3.2.3 Infrared Band Assignment of the CO₂ Hydrogenation Adsorbed Species on Ni-USY

In this section, the IR absorption spectra of CH₄, CO₂, CO and transient species adsorbed on Ni-USY are discussed. The references for the adsorbed species are presented in Table 2. The total volumetric flow was set to 20 NmL min⁻¹ with the following gas composition: 2 NmL CO₂ min⁻¹; 8 NmL H₂ min⁻¹ and 10 NmL Ar min⁻¹. Conventional IR measurements (32 cm⁻¹ resolution) were performed with

and without plasma assistance. Fig. 4 shows the following three spectra: (a) the zeolite Ni-USY wafer only; (b) the zeolite Ni-USY wafer together with the reactants (CO₂ and H₂) and (c) the zeolite Ni-USY wafer together with the plasma-assisted CO₂ hydrogenation products which are present in the gas phase and also over the catalyst surface. The absence of a broad IR band between 4000 and 3750 cm⁻¹ shows a correct dehydration of the catalyst samples indicating a good vacuum system operation. The IR bands between 2100 and 1500 cm⁻¹ represent the adsorbed species as well as the

Table 2 IR band assignments of plasma-assisted CO₂ hydrogenation adsorbed species on Ni-USY

Adsorbed species	Mode	Band position (32 cm ⁻¹ resolution)	Ref.
Monodentate formates on nickel	ν C=O	1561	[39]
Adsorbed water on zeolite framework	δ O-H	1634	[40]
Zeolite band		1696	This work
Zeolite band		1777	
Zeolite band		1872	
Linear carbonyls on nickel	ν C=O	1989–1995 (shift)	[41]
Nickel dicarbonyl Ni(CO) ₂	ν C=O	2118	
N-CH	ν C-H	2740	[42]
Ni-CH ₂	ν C-H	2812	
Ni-CH ₃	ν C-H	2864	
H bonding surface water OH groups	ν O-H	3173	[40]
H bonding zeolite oxygen atoms	ν O-H	3252	

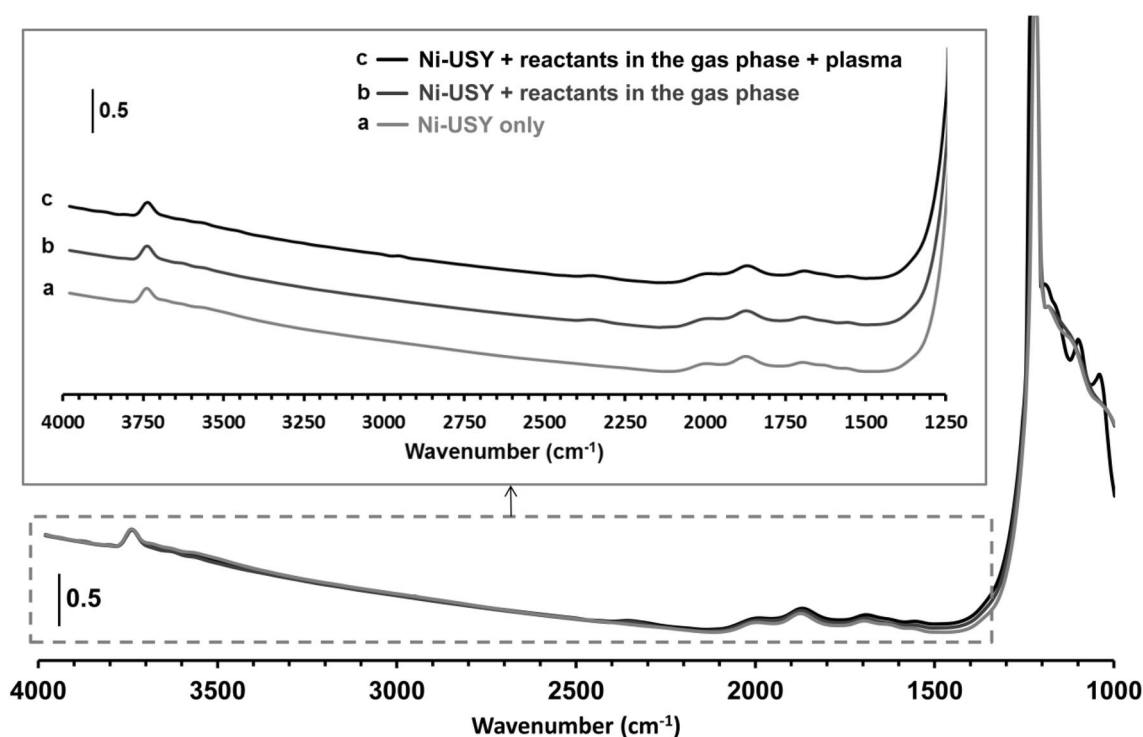


Fig. 4 IR bands of CO₂ hydrogenation species over Ni-USY with and without plasma assistance

Ni-USY zeolite IR bands. The intensities of the three IR spectra are saturated at 1200 cm^{-1} . This fact indicates that the catalyst wafer did not present any orifice (not perforated). Lower wavenumbers (below 1000 cm^{-1}) cannot be observed with the MCT detector used.

The IR band at 3742 cm^{-1} corresponding to silanol groups (Si–OH) of the USY zeolite support was observed in the three spectra.

The IR bands of the adsorbed species generated during the plasma-assisted CO_2 hydrogenation reaction can be assigned from the difference between the IR light intensity of the curves c and b (Fig. 5).

The different regions of the difference IR spectrum will be analyzed in detail.

3.2.3.1 IR Region Between 4000 and 3300 cm^{-1} The dark gray negative bands in Fig. 5 correspond to different sorts of OH groups that are suppressed after plasma ignition. In this region, elongation vibrations in OH groups are basically found. There are several parameters influencing the frequency of the $\nu(\text{OH})$ bands such as the coordination number of the oxygen atom, the presence of cationic vacancies in the direct vicinity of the OH group, the oxidation state of the cation [43] indicating that their band frequencies can be shifted depending on the catalyst under study.

The IR band at 3425 cm^{-1} corresponds to the stretching of OH groups of adsorbed molecular water. The IR bands at

3518 and 3682 cm^{-1} are assigned to OH groups on nickel in the sodalite cages and in the exchange positions respectively. The bands at 3723 and 3754 cm^{-1} are assigned to the vibration of very weakly acidic isolated silanol groups. Finally, the very high frequency band at 3867 cm^{-1} can be attributed to the antisymmetric stretching of OH groups of H_2O moiety in the faujasite channels [44].

3.2.3.2 IR Region from 3300 to 2700 cm^{-1} and From 2500 to 2150 cm^{-1} The difference IR spectrum between 3300 and 2700 cm^{-1} is presented in Fig. 6a.

The IR bands at 2740 , 2812 and 2864 cm^{-1} correspond to CH, CH_2 and CH_3 species adsorbed on metallic nickel respectively. The IR bands at 3069 , 3019 and 2950 cm^{-1} are assigned to CH_4 in the gas phase. The bands at 3173 and 3252 cm^{-1} are due to H-bonded OH groups.

The difference IR spectrum between 2500 and 2150 cm^{-1} is presented in Fig. 6b. The IR absorption bands in this region correspond to the reactants and products of CO_2 hydrogenation in the gas phase. The band at 2345 and 2293 cm^{-1} are assigned to ground state and vibrationally excited CO_2 molecules respectively. The band at 2191 cm^{-1} is attributed to CO in the gas phase. It is worth noticing that this IR band was not previously assigned to CO gas in Table 1 (2165 and 2120 cm^{-1}). These two bands are observed here as one band only as a consequence of the difference spectra low resolution (32 cm^{-1}). Besides, this band

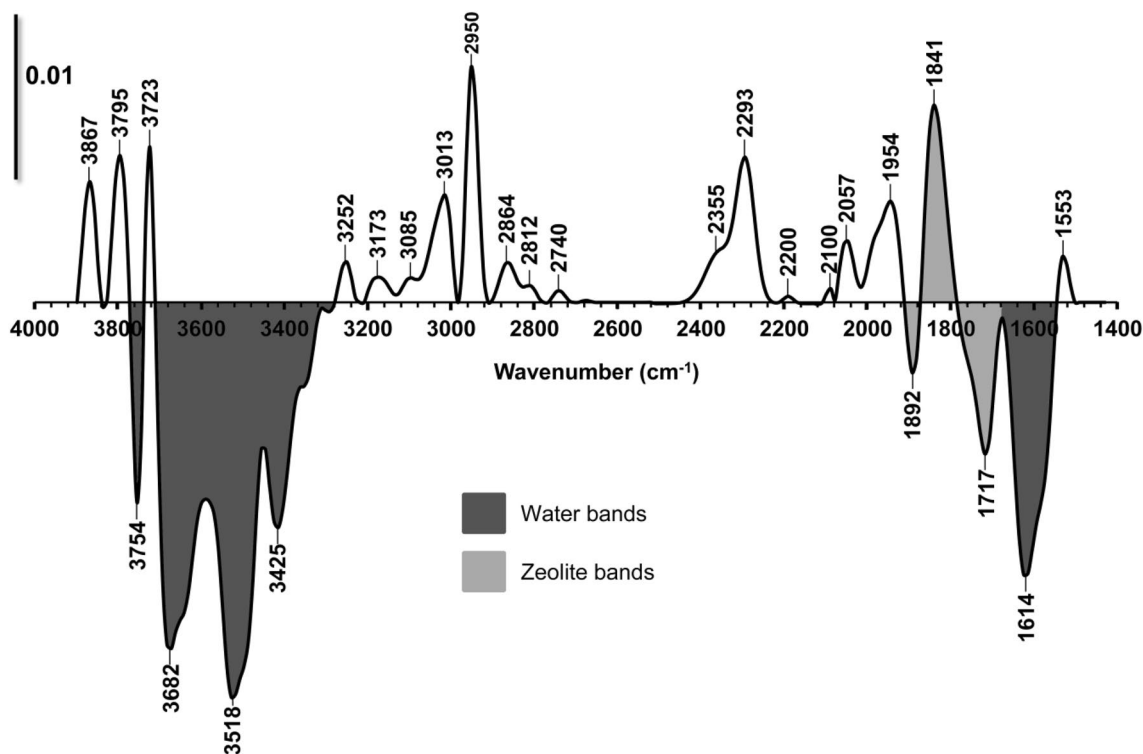


Fig. 5 Difference IR spectrum (with plasma minus without plasma) showing adsorbed species on Ni-USY

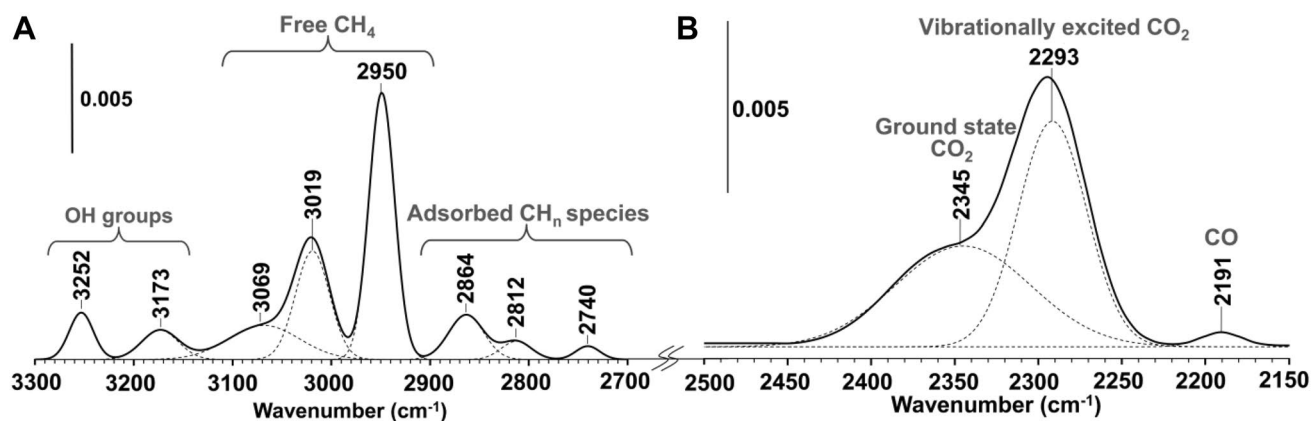


Fig. 6 **a** Difference IR spectrum between 3300 and 2700 cm^{-1} ; **b** difference IR spectrum between 2500 and 2150 cm^{-1}

is shifted towards higher frequencies due to the temperature effect. The spectra before and during plasma (b and c spectra of Fig. 4) have been recorded at different temperatures. An average temperature of 125 °C in the wafer (curve c) has been determined, under plasma irradiation against room temperature for the spectrum without plasma (curve b). Nevertheless, IR band shift has been observed for the case of CO molecules in the gas phase. This shift, observed in the gas phase, does not affect the interpretation and assignment of the adsorbed species.

It is worth noticing that a CO_2 ground state positive signal in the difference IR spectrum of Fig. 6b is observed, which seems to contradict Fig. 3, in which CO_2 ground state decreases after plasma ignition as a consequence of the CO_2 dissociation into CO in the gas phase. The amount of ground state CO_2 is not higher with plasma than without. Nevertheless, when the catalyst wafer is put in contact with the gas, which is flowing at high speed (very high Reynolds number) and at higher temperature (plasma ON), a relatively low fluid dynamics problem arises in our IR cell. This problem does not have any influence on the adsorbed species. Vortex can be formed around the obstacle (wafer) and a concentration increase of the mixture compound with the highest dynamic viscosity can be experienced. Gas viscosity increases with temperature (if the pressure is kept constant). In our mixture, CO_2 viscosity was calculated to be 1.4 times the hydrogen viscosity. In other words, CO_2 is being retained around the wafer while hydrogen flows away from the IR beam with a lower resistance. CFD simulations will be performed in our IR Operando plasma cells in order to determine the vorticity and local velocity fields around the catalyst wafer. Notice also that this problem, with ground state CO_2 , is not observed during IR Time-resolved measurements at lower temporal resolution (ms).

3.2.3.3 IR Region Between 2150 and 1400 cm^{-1} The IR absorption bands of zeolite USY as well as those cor-

responding to CO_2 hydrogenation adsorbed intermediates species can be found in this IR region between 2150 and 1400 cm^{-1} .

In order to distinguish the bands of zeolite USY and those of intermediate species adsorbed on the catalyst surface, the intensity of all bands was followed during the CO_2 hydrogenation reaction assisted by plasma (Fig. 7).

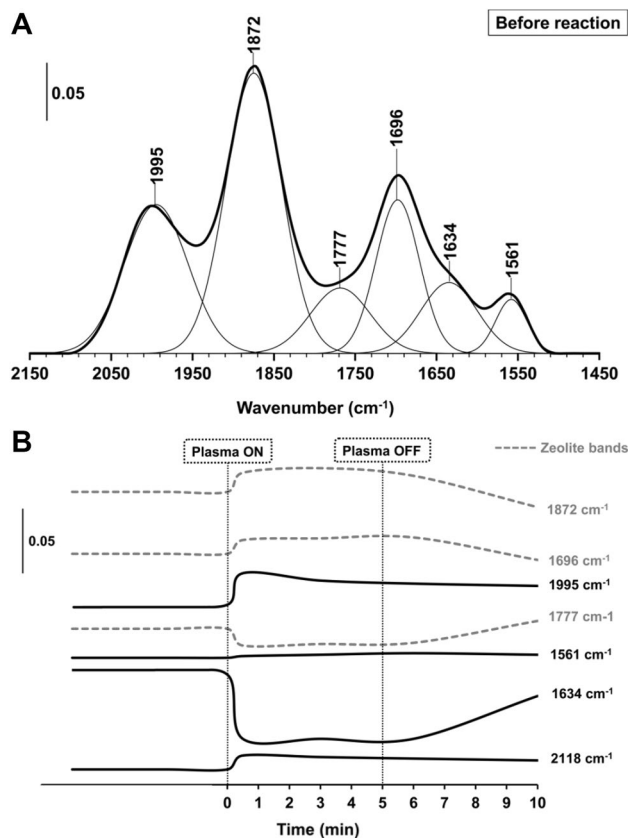


Fig. 7 IR absorption bands of zeolite USY and adsorbed intermediates species

The spectra were recorded before starting the reaction, during the reaction, right after plasma extinction and 3 and 5 min after the plasma extinction. The evolution of the intensity of all the IR bands in this region was analyzed after IR bands decomposition. The different IR bands of zeolite USY and adsorbed intermediates species before starting the reaction are showed in Fig. 7a. The different spectra showing the evolution of the IR bands intensity as a function of time can be consulted in supplementary files. The temporal evolution of the IR bands intensity can be observed in Fig. 7b.

The band at 1634 cm^{-1} is assigned to the bending vibration of OH groups of surface water molecules adsorbed on zeolite. This band is suppressed after plasma ignition indicating that the water molecules are easily desorbed from the zeolite surface by plasma. When the glow discharged is initiated, the intensity of the band at 1995 cm^{-1} is increased as a consequence of CO adsorption on metallic nickel. This band is assigned to CO stretching mode of linear carbonyls groups over nickel. When the plasma is stopped, this band is shifted towards lower frequencies indicating a decrease of nickel surface coverage by CO. After plasma ignition, a new IR absorption band appears at 2118 cm^{-1} . This band is attributed to CO stretching mode of more stable dicarbonyls species on nickel which are formed from the linear carbonyls. Nickel dicarbonyls actually present two IR bands: a first band at $2145\text{--}2131\text{ cm}^{-1}$ due to the CO symmetric stretching vibration and a second band at $2100\text{--}2081\text{ cm}^{-1}$ due to the CO antisymmetric stretching vibration. Since low resolution (32 cm^{-1}) is used, only one IR band located at 2118 cm^{-1} is observed. The IR band at 1561 cm^{-1} increases under plasma as a consequence of the adsorption of CO_2 molecules on nickel. This band corresponds to CO stretching mode of monodentate formates on nickel. The IR bands at 1872 , 1696 and 1777 cm^{-1} are attributed to zeolite USY bands. When plasma is ignited, the intensities of the first two bands increase while the one at 1777 cm^{-1} decreases. This observation is inverted after plasma extinction indicating that the temporal evolutions of the IR intensity of these three bands are closely related. In fact, these IR absorption bands represent the contraction and expansion of the zeolite USY framework under plasma irradiation as a consequence of the adsorption and desorption processes inside the zeolite cavities.

The IR band assignments of the adsorbed species on Ni-USY are summarized in Table 2.

Figure 7 shows that the intensity increase of the IR band at 1561 cm^{-1} corresponding to monodentate formates, as a consequence of CO_2 molecules adsorbed on nickel, is significantly lower than those observed in the case of IR bands at 1995 and 2118 cm^{-1} assigned to adsorbed CO molecules as carbonyls. Carbon adsorbed species are mainly represented by carbonyls species rather than

formates species. CO_2 molecules can mainly contribute to methane production after dissociation by plasma in the gas phase into CO molecules.

3.2.4 Microsecond Time-Resolved FTIR Spectroscopy (Step Scan)

The temporal evolution (microsecond) of the IR band intensities acquired with step scan FTIR for the free and adsorbed species summarized in Tables 1 and 2 are presented in Fig. 8. A reaction mechanism can be proposed to account for the observations.

The CO_2 dissociation into CO by plasma is shown in Fig. 8a. CO_2 molecules are vibrationally excited by plasma and further dissociated into CO in the gas phase. This fact can be evidenced by the decrease of the IR intensity at 2345 cm^{-1} and the increase in intensity of the IR band at 2293 cm^{-1} when CO_2 molecules are exposed to a plasma pulse (indicated here by a vertical gray line). The intensity curve of the IR band at 2293 cm^{-1} corresponding to the vibrationally excited CO_2 molecules is 180° phase-shifted relative to the CO_2 ground state molecules trace at 2345 cm^{-1} and this event is repeated through the three plasma periods from 0 to 60 ms. The intensity curve of the IR band at 2191 cm^{-1} corresponding to CO molecules is 180° phase-shifted relative to the vibrationally excited CO_2 molecules at 2293 cm^{-1} . Therefore, after the plasma pulse, the excited CO_2 molecules are dissociated into CO molecules in the gas phase. In the presence of the Ni-USY catalyst, the vibrationally excited CO_2 molecules can be also adsorbed on nickel. The IR intensity curve at 1561 cm^{-1} , corresponding to monodentate formates on metallic nickel, increases while the IR intensity trace at 2293 cm^{-1} (Excited CO_2 molecules) decreases (Fig. 8b). The adsorbed CO_2 molecules on nickel as monodentate formates are further transformed into linear carbonyls under plasma assistance (Fig. 8b). When the plasma is ignited (vertical gray line), the IR intensity at 1561 cm^{-1} decreases while the one at 1989 cm^{-1} corresponding to linear carbonyls is increased. Between two plasma pulses, more stable dicarbonyl species on metallic nickel (IR band at 2118 cm^{-1}) can be formed from linear carbonyls (Fig. 8b, c).

With the same reasoning, one can propose from Fig. 8c that linear carbonyls (1989 cm^{-1}) are hydrogenated to form CH species on nickel (2740 cm^{-1}), which are then hydrogenated to give CH_2 (2812 cm^{-1}) and CH_3 species (2864 cm^{-1}) on nickel (Fig. 9d). CH_3 species are finally hydrogenated into CH_4 molecules (2958 cm^{-1}) which are further desorbed from the catalyst (Fig. 8d). The plasma-assisted CO_2 hydrogenation mechanism is summarized in Fig. 9.

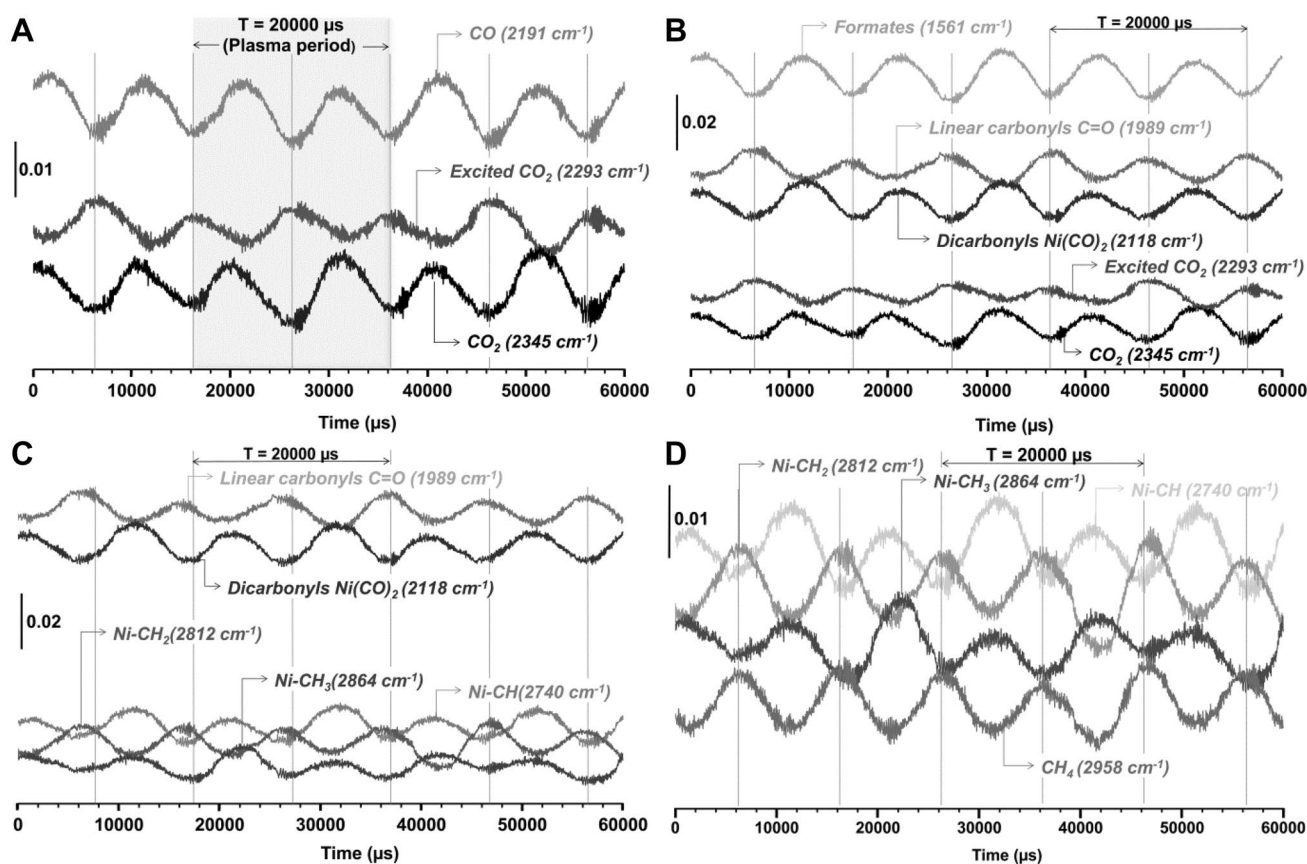


Fig. 8 Temporal evolution of free and adsorbed species IR band intensities (Step Scan)

4 Gas Versus Surface Reactions

In the absence of catalyst, CO_2 molar conversion is 60% under plasma assistance with 99% CO molar selectivity. In glow discharge plasmas, the CO_2 dissociation is mainly caused by electron impact [45]. Hence, without catalyst, CO molecules are produced from CO_2 dissociation in the gas phase only. A relatively low amount of CH_4 can also be generated in the gas phase but CH_4 production can only be enhanced with the presence of an appropriate catalyst. In this article, we studied the CO_2 hydrogenation reaction mechanism using the most efficient catalyst determined from a previous study: Ni-USY (14% wt. Ni).

In the presence of the catalyst, CO_2 molar conversion is still 60% under plasma assistance but with a higher amount of CH_4 produced with respect to the reaction carried out without catalyst. Actually, the reduced nickel particles, located outside the zeolite crystallites, are the real active sites on which the methane formation will take place. It is worth noticing that this catalyst shows a bimodal Ni distribution. It is formed mainly of large nickel particles (metallic nickel after reduction) as well as of nickel ions (Ni^{2+}) located within the exchange position inside the zeolite cavities. Nickel ions were evidenced by

hydrogen consumption at relatively high temperatures during the TPR-MS (T above 700°C). The site responsible for the catalytic reaction activity is then the metallic nickel large particles (Ni^0) which are located outside zeolite pores. In plasma-catalysis, when using porous catalysts, it is very important to determine if the plasma is being generated inside the catalyst pores in order to define the real active surface of the catalyst. In our study, the active phase is located on the catalyst surface only and represented by the reduced metallic nickel particles (Ni^0) which are located outside the zeolite pores. However, the plasma reactions observed in the gas phase only, could be present inside the zeolite pores (microdischarges) if the plasma can be generated inside them. Zhang et al. [46] have performed a very interesting modeling investigation about the influence of the materials dielectric constant, ranging from 4 to 1000, on the possibility of plasma formation inside pores. They have shown that materials with lower dielectric constant allow plasma formation inside smaller pores than materials with higher dielectric constant. Authors concluded that in the case of the most common catalyst supports such as Al_2O_3 and SiO_2 with dielectric constants around $\epsilon_r = 8 - 11$ and 4.2 respectively (lower side of the dielectric constant range studied in [46]) should enhance the probability of microdischarges

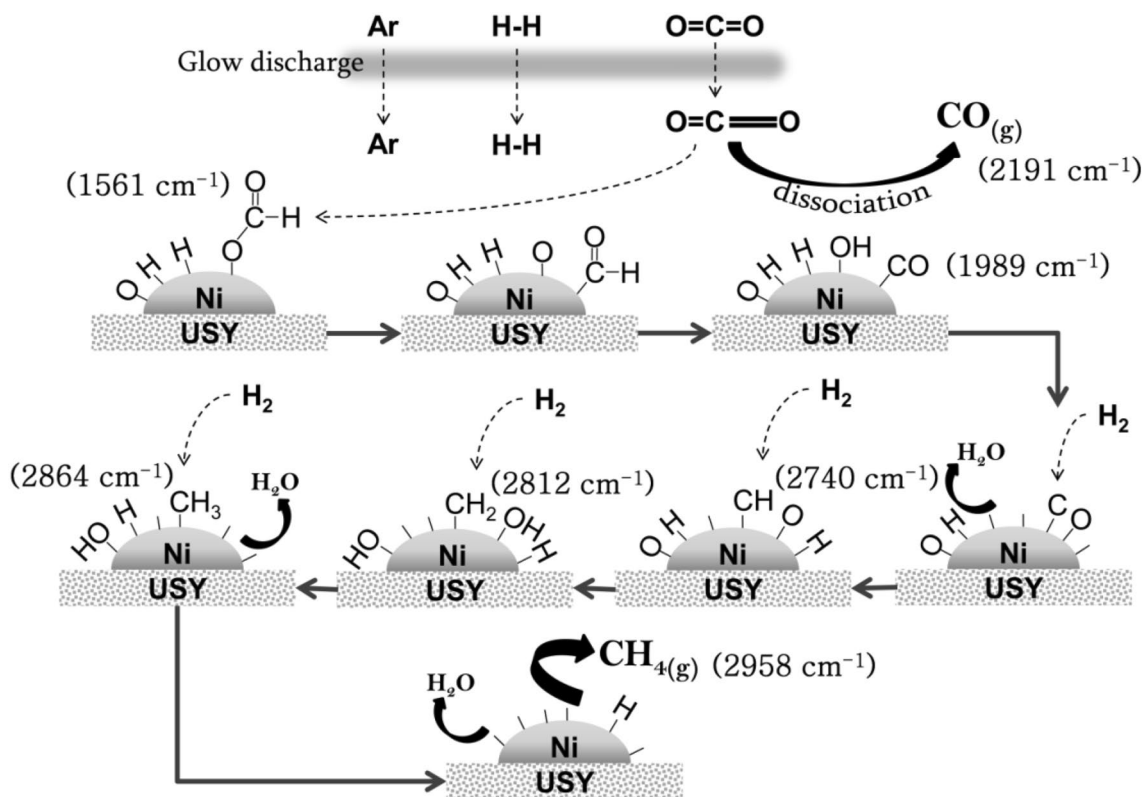


Fig. 9 Proposed plasma-assisted CO₂ hydrogenation mechanism over Ni-USY zeolite

generation inside the material pores, even for smaller pore sizes. Despite the fact that the USY catalyst used in this work presents a relatively low dielectric constant [47] with respect to the dielectric constant range studied in [46], it is difficult to ensure plasma formation inside our USY catalyst pores as a consequence of the large difference in the order of magnitude of the pores (more than three orders of magnitude smaller than those studied in [46]). Moreover, plasma generation inside the USY pores could be restricted since the sidewall effects described in [46] would become much more important in nanosized pores.

Zhang et al. [48] have also modelled the applied voltage and the pore size in the formation of microdischarges in atmospheric DBD helium plasma. Authors concluded that plasma formation inside pores is only possible for pores sizes in the micrometer range. In fact, plasma can only exist inside the pores if the Debye length is lower than the average USY zeolite pore diameter. In our work, we used a 2 kV glow discharge with a relatively high electron density ($\approx 10^{17} \text{ m}^{-3}$) and an electron temperature $T_e \approx 3 \text{ eV} (=3.48 \times 10^4 \text{ K})$. If the ion temperature is neglected with respect to the electron temperature, Debye length can be estimated by Eq. (1):

$$\lambda_D = \sqrt{\frac{\epsilon_0 \times k_B \times T_e}{n \times e^2}} \quad (1)$$

where λ_D is the Debye length, ϵ_0 is the permittivity of free space ($8.85 \times 10^{-12} \text{ F m}^{-1}$), k_B is the Boltzmann constant ($1.38 \times 10^{-23} \text{ J K}^{-1}$), e is the charge of an electron ($1.6 \times 10^{-19} \text{ C}$), T_e is the temperature of the electrons (K), n is the density of electrons (m^{-3}).

For our USY zeolite, the Debye length would then be equal to 40.74 μm which is three orders of magnitude larger than the USY pore size. This fact would still indicate that plasma cannot be formed inside our zeolite pores. In reactive gases, where filaments can be formed, characterized by higher electron density, plasma formation might be possible in sub-micrometer pores. Nevertheless, in this work, a 2 kV glow discharge has been used and these filaments are not present. However, reactive species from the bulk plasma phase can diffuse inside the sub-meter pores (nanometer sized pores) and interact with the inner walls of the USY pores. El-Roz et al. [49] stated that plasma can be formed at the core of zeolites. Nevertheless, this is probably wrong, and the zeolite modification by plasma quoted by the authors could be simply explained by reactive species diffusion from the bulk plasma phase inside their zeolite pores.

The generation (or not) of the plasma inside the USY pores, however, does not affect the mechanism proposed in this study since CO₂ hydrogenation takes place on the catalyst surface only.

Since the initial form of the parent zeolite support was protonic (H-USY) and the Si/Al molar ratio of the Ni-USY was relatively high (Si/Al=40), CO₂ was not adsorbed on zeolite as carbonates. Therefore, the CH₄ formation from carbonates as intermediate should be discarded. CO and vibrationally excited CO₂ molecules in the gas phase are accommodated by metallic nickel particles located at the zeolite surface only. Formates (from CO₂) and carbonyls (from CO) were observed during the reaction over metallic nickel. It was observed that formates are transformed to CO over metallic nickel particles indicating that CO is the real intermediate in the CH₄ formation from CO₂ under plasma assistance. These results are in agreement with those found for the same catalyst but under conventional heating without plasma assistance [1].

5 Conclusions

The mechanism of plasma-assisted CO₂ hydrogenation was studied by Operando time-resolved FTIR spectroscopy. Carbon monoxide was detected as the main product of the reaction as a consequence of CO₂ dissociation in the gas phase by the glow discharge. Methane was also observed as a secondary product. It remained in low amounts since the reaction was carried out under partial vacuum: pressure was kept low in order to promote the plasma discharge and to enhance its energy in the gas phase. Methane selectivity is also reduced by the fact that CO molecules, which are produced in the gas phase by plasma CO₂ dissociation, are being adsorbed on nickel thus covering the active phase surface and reducing its activity for CH₄ production. When the plasma is stopped, the IR band of adsorbed CO molecules is shifted towards lower frequencies indicating a decrease in nickel surface coverage which actually favors the methane production.

Protonic Ni-USY was used as a catalyst. This zeolite presents no significant basic behavior and vibrationally excited CO₂ molecules are then adsorbed on nickel forming formates rather than carbonates. Carbonyls generated from adsorption of CO molecules produced after CO₂ plasma dissociation (major contribution) as well as from formates species are consecutively hydrogenated to form CH, CH₂ and CH₃ species on nickel, which were precisely detected using FTIR. Finally, CH₄ and H₂O are formed and desorbed from the nickel surface.

Further studies will try to improve methane selectivity in plasma-assisted CO₂ hydrogenation. This could be achieved by limiting CO coverage of nickel, for example with shorter plasma pulses. Besides, the use of pulsed discharges will enhance the energy efficiency of the plasma process. The mechanism will also be studied with Operando time-resolved FTIR spectroscopy in the more popular dielectric-barrier

(DBD) plasma. The mechanism is expected to be different as a consequence of the different (filamentary) nature of DBD plasma and of the different species population generated in the gas phase.

References

1. Westermann A, Azambre B, Bacariza MC, Graça I, Ribeiro MF, Lopes JM, Henriques C (2015) *Appl Catal Environ B* 174:175–175, 120–125
2. Khodakov AY, Chu W, Fongarland P (2007) *Chem Rev* 107:1692–1744
3. Raje AP, Davis BH (1997) *Catal Today* 36, 335–345
4. Dry ME (1999) *Appl Catal A* 189:185–190
5. Dry ME (2002) *Catal Today* 71:227–241
6. Fan Z, Sun K, Rui N, Zhao B, Liu C-j. (2015) *J Energy Chem* 24:655–659
7. Wanga W, Chu W, Wang N, Yang W, Jiang C (2016) *Int J Hydrog Energy* 41:967–975
8. Duyar MS, Ramachandran A, Wang C, Farrauto RJ (2015) *J CO2 Util* 12:27–33
9. Xu J, Lin Q, Su X, Duan H, Geng H, Huang Y (2016) *Chin J Chem Eng* 24:140–145
10. Bahruji H, Bowker M, Hutchings G, Dimitratos N, Wells P, Gibson E, Jones W, Brookes C, Morgan D, Lalev G, *Catal J* (2016) *J Catal.* doi:10.1016/j.jcat.2016.03.017
11. Kattel S, Yan B, Chen JG, Liu P (2016) *J Catal.* doi:10.1016/j.jcat.2015.12.019
12. Büchel R, Baiker A, Pratsinis SE (2014) *Appl Catal A* 477:93–101
13. Chen Y, Choi S, Thompson LT (2016) *J Catal.* doi:10.1016/j.jcat.2016.01.016
14. Hartadi Y, Widmann D, Behm RJ (2016) *J Catal* 333:238–250
15. Lei H, Nie R, Wu G, Hou Z (2015) *Fuel* 154:161–166
16. Ussa Aldana PA, Ocampo F, Kobl K, Louis B, Thibault-Starzyk F, Daturi M, Bazin P, Thomas S, Roger AC (2013) *Catal Today* 215:201–207
17. Abelló S, Berruero C, Montané D (2013) *Fuel* 113:598–609
18. Kameshima S, Tamura K, Ishibashi Y, Nozaki T (2015) *Catal Today* 256:67–75
19. Nozaki T, Okazaki K (2013) *Catal Today* 211:29–38
20. Neyts EC, Ostrikov K, Sunkara MK, Bogaerts A (2015) *Chem Rev* 115:13408–13446
21. Neyts EC (2016) *Plasma Chem Plasma Process* 36:185–212
22. Neyts EC, Bogaerts A (2014) *J Phys D* 47:224010
23. Whitehead JC (2016) *J Phys D* 49:243001
24. Ren J, Guo H, Yang J, Qin Z, Lin J, Li Z (2015) *Appl Surf Sci* 351:504–551
25. Beuls A, Swalus C, Jacquemin M, Heyen G, Karelovic A, Ruiz P (2012) *Appl Catal B* 113–114:2–10
26. Miao B, Khine Ma SS, Wang X, Su H, Hwa Chan S (2016) *Catal Sci Technol* 6:4048–4058
27. Rönsch S, Schneider J, Matthischke S, Schlüter M, Götz M, Lefebvre J, Prabhakaran P, Bajohr S (2016) *Fuel* 166:276–296
28. Avanesian T, Gusmão GS, Christopher P (2016) *J Catal.* doi:10.1016/j.jcat.2016.03.016
29. Wang X, Hong Y, Shi H, Szanyi J (2016) *J Catal.* doi:10.1016/j.jcat.2016.02.001
30. Weatherbee GD, Bartholomew CH (1982) *J Catal* 77:460–472
31. Tada S, Kikuchi R (2015) *Catal Sci Technol* 5:3061–3070
32. Fujita S.-I., Nakamura M, Doi T, Takezawa N (1993) *Appl Catal A* 104:87–100
33. Garbarino G, Riani P, Magistri L, Busca G (2014) *Int J Hydrog Energy* 39:11557–11565

34. Pan Q, Peng J, Sun T, Wang S, Wang S (2014) *Catal Commun* 45:74–78
35. Kim HY, Lee HM, Park J-N (2010) *J Phys Chem C* 114:7128–7131
36. Mei D, Zhu X, Wu C, Ashford B, Williams PT, Tu X (2016) *Appl Catal B* 182:525–532
37. Chen G, Georgieva V, Godfroid T, Snyders R, Delplancke-Ogletree M-P (2016) *Appl Catal B* 190:115–124
38. Rivallan M, Aiello S, Thibault-Starzyk F (2010) *Rev Sci Instrum* 81:103111
39. Haq S, Love JG, Sanders HE, King DA (1995) *Surf Sci* 325:230–242
40. Thibault-Starzyk F, Maugé F (2012) Infrared spectroscopy. In: Che M, Védrine J (eds) *Characterization of solid materials and heterogeneous catalysts: from structure to surface reactivity*, pp 3–48. Wiley, New Jersey
41. Hadjiivanov KI, Vayssilov GN (2002) *Adv Catal* 47:307–511
42. Hayes RE, Thomas WJ, Hayes KE (1983) *Appl Catal* 6:653–659
43. Thibault-Starzyk F, Maugé F (2012) *Infrared spectroscopy in characterization of solid materials and heterogeneous catalysts: from structure to surface reactivity*, 1st edn, Che M, Vedrine JC (eds). Wiley, New Jersey
44. Jungsuttiwong S, Limtrakul J, Truong TN (2005) *J Phys Chem B* 109:13342–13351
45. Fridman A (2008) *Plasma Chemistry*. Cambridge University Press, Cambridge
46. Zhang YR, Neyts EC, Bogaerts A (2016) *J Phys Chem C* 120:25923–25934
47. Azzolina Jury F, Polaert I, Estel L, Pierella LB (2013) *Appl Catal A Gen* 453:92–101
48. Zhang YR, Van Laer K, Neyts EC, Bogaerts A (2016) *Appl Catal B* 185:56–67
49. El-Roz M, Lakiss L, Vicente A, Bozhilov KN, Thibault-Starzyk F, Valtchev V (2014) *Chem Sci* 5:68–80